Nonlinear Atmospheric Adjustment to Thermal Forcing

PAUL F. FANELLI AND PETER R. BANNON

Department of Meteorology, The Pennsylvania State University, University Park, Pennsylvania

(Manuscript received 3 August 2004, in final form 28 January 2005)

ABSTRACT

A nonlinear, numerical model of a compressible atmosphere is used to simulate the hydrostatic and geostrophic adjustment to a localized prescribed heating applied over five minutes with a size characteristic of an isolated, deep, cumulus cloud. This thermal forcing generates both buoyancy waves and a horizontally propagating Lamb wave packet as well as a steady state rich in potential vorticity. The adjustments in three model atmospheres (an isothermal, a constant lapse rate, and one with a stratosphere) are studied.

The Lamb wave packet and the two lowest-order buoyancy waves are relatively unaffected by nonlinearities but the higher-order modes and the steady state are. The heating generates a vertically stacked dipole of potential vorticity with a cyclonic perturbation below an anticyclonic perturbation. In contrast to the linear results, the nonlinear dipole is severely distorted by vertical and horizontal advections. In addition, the Lamb wave packet contains some weak positive perturbation potential vorticity.

The energetics is examined using traditional and Eulerian available energetics. Traditional energetics consists of kinetic, internal, and potential energies. It is shown that the Lamb wave packet contains more total traditional energy than that input to the atmosphere by the heating. The traditional energy in the packet resides primarily in the form of internal energy and only secondarily in the form of potential energy. The passage of the Lamb wave packet produces an atmosphere that, overall, is cooler, less dense, and with less total traditional energy than the initial atmosphere. Eulerian available energetics consists of kinetic, available potential, and available elastic energies. The heating generates both available elastic and potential energy that is then converted into kinetic energy. Most of the available elastic energy projects onto the Lamb packet, while almost all of the available potential energy is associated with the buoyancy waves and the steady state.

The effects of varying the spatial and temporal scale of the heating, while keeping the net heating the same, are examined. As the duration of the heating decreases, the amount of energy projected onto the waves increases. Increasing the size of the heating decreases the amount of energy projected onto the waves.

The adjustment is kinetically more vigorous in the nonisothermal atmospheres because of the reduction in the base-state static stability. The presence of a stratosphere produces large anomalies at and above the tropopause that are linked to the vertical motions of the buoyancy wave field.

1. Introduction

A variety of perturbations frequently force the compressible atmosphere out of its approximate hydrostatic and geostrophic state. The atmosphere must adjust to these imbalances toward a new equilibrium state. This atmospheric adjustment process involves the generation of both buoyancy and acoustic modes that act to redistribute mass, momentum, and entropy so that a new balance is reached. Chagnon and Bannon (2005a) provide a recent survey of the literature.

Corresponding author address: Peter R. Bannon, Dept. of Meteorology, The Pennsylvania State University, University Park, PA 16802.
E-mail: bannon@ems.psu.edu

Chagnon and Bannon (2001) modeled linear geostrophic and hydrostatic adjustment in a two-dimensional atmosphere. They examined the available energetics of the initial and final equilibrium states and found that the heating initially generates available elastic and potential energies. Chagnon and Bannon (2005a,b) used an analytic linear model to simulate the wave response during atmospheric adjustment to various types of forcings. They examined transient dynamics and partitioned the energy generated by the forcing between buoyancy, acoustic, and Lamb waves, as well as the steady state. A long-duration heating suppresses vertically propagating acoustic modes, but generates buoyancy waves and a horizontally propagating wave of compression, called a Lamb wave. A short-duration

heating also produces vertically propagating acoustic modes; however, Chagnon and Bannon (2005b) found that once the duration of the heating exceeds the period of the acoustic cutoff (~300 s), almost no energy is projected onto these modes.

In contrast to these linear analyses in isothermal atmospheres, the purpose of this study is to simulate atmospheric adjustment to a localized, finite-amplitude heating of finite duration using a fully compressible, nonlinear, numerical model of nonisothermal atmospheres. The analysis of the adjustment process includes an examination of the flow fields, the potential vorticity distribution, and the energetics of the adjustment. In the present study, a heating of sufficiently long duration is used so that it suppresses the vertically propagating acoustic waves.

Because the model is nonlinear, two different formulations of the energetics consistent with nonlinear theory are examined. Traditional nonlinear energetics is the sum of the kinetic, potential, and internal energies. In contrast, Eulerian available energetics (Bannon 2005) is the sum of the kinetic and available potential and elastic energies. The concept of available energy was first developed in a meteorological context by Dutton (1973), who developed a global quantity, called entropic energy, which he used to diagnose atmospheric energetics. It is described as the amount of energy available to be converted into kinetic energy. Kucharski (1997) called this available energy exergy. Recently, Bannon (2005) derived local available energetics from an Eulerian perspective for a multiphase, compressible, fluid system.

Section 2 describes the model atmosphere and numerical techniques. Section 3 describes the concepts underlying and equations for traditional and Eulerian available energy. It is shown that the Eulerian available energy allows one to make direct comparisons of available energetics between linear and nonlinear models. Section 4 presents the numerical solutions to a heating of finite spatial and temporal structure in an isothermal atmosphere. The effects of nonlinearities compared to the linear analyses are delineated. Section 5 describes solutions in nonisothermal atmospheres and compares them to the isothermal case of section 4. Section 6 presents a summary and concluding remarks.

2. The numerical model

a. Governing equations

The model atmosphere is a compressible, dry, inviscid, rotating atmosphere on an f plane. The governing equations in Cartesian coordinates are

$$\frac{\partial \mathbf{u}}{\partial t} = -(\mathbf{u}\cdot\nabla)\mathbf{u} - c_p\theta\nabla\pi - f\mathbf{k}\times\mathrm{u} - g\mathbf{k}, \quad (2.1)$$

$$\frac{\partial \theta}{\partial t} = -\mathbf{u}\cdot\nabla\theta + \Theta, \quad (2.2)$$

$$\frac{\partial \pi}{\partial t} = -\mathbf{u}\cdot\nabla\pi + \pi\frac{R}{c_v}\nabla\cdot\mathbf{u}, \quad (2.3)$$

$$T = \theta\pi, \quad (2.4)$$

$$p = \rho RT, \quad (2.5)$$

where f is the Coriolis parameter, g is the acceleration due to gravity, ∇ is the three-dimensional del operator, and $\mathbf{k}$ is the unit vector in the z direction. The variables $\mathbf{u}$, ρ, p, θ, and T are the three-dimensional velocity vector, the density, the pressure, the potential temperature, and the temperature. The constants R, c_p, and c_v are the ideal gas constant and the specific heats of dry air at constant pressure and constant volume. The nondimensional pressure is defined as

$$\pi \equiv \left(\frac{p}{p_{00}}\right)^{R/c_p}, \quad (2.6)$$

where $p_{00} = 1000$ hPa. The last term in (2.2) is a prescribed diabatic warming rate. Equations (2.1)–(2.3) are prognostic equations for the velocity, potential temperature, and nondimensional pressure and form a closed system of equations. Equations (2.4)–(2.6) are diagnostic equations for the temperature, density, and pressure.

b. Thermal forcing

The model atmosphere is forced with the prescribed two-dimensional warming on the right-hand side of the potential temperature equation (2.2) with the form

$$\Theta = \frac{2\theta\delta Q F(t)G(z)H(x)}{\rho c_p T\tau}, \quad (2.7)$$

where τ is the duration of the heating, δQ is its amplitude per unit volume, and F, G, and H are functions describing its temporal, vertical, and horizontal structure. The forcing structure in the horizontal is

$$H(x) = \begin{cases} \cos^2\left(\pi\dfrac{x}{2a}\right), & 0 \le x \le a \\ 0, & x > a \end{cases} \quad (2.8)$$

and that in the vertical is

$$G(z) = \begin{cases} \cos^2\left(\pi \dfrac{z - h - d/2}{d}\right), & h \le z \le h + d \\ 0, & z < h \quad \text{and} \quad z > h + d. \end{cases} \tag{2.9}$$

Here a is the horizontal width of the heating, h is the height of the heating above the surface, and d is the vertical depth of the heating. The forcing is applied over a finite duration with the temporal structure

$$F(t) = \begin{cases} \sin^2\left(\pi \dfrac{t}{\tau}\right), & t \le \tau \\ 0, & t > \tau. \end{cases} \tag{2.10}$$

The factor of $2/\tau$ in (2.7) ensures that the integral over time t from $t = 0$ to $t = \tau$ yields a net heating given by $\delta Q\ G\ (z)\ H\ (x)$. The cosine-squared horizontal and vertical structures prevent infinite pressure gradients from forming at the boundaries of the heated region. The sine-squared temporal structure is chosen because it produces smooth fields and both it and its first derivative are continuous functions of time. Furthermore it naturally filters out vertically propagating acoustic waves that form as a result of the sudden change in heating rate associated with a top-hat temporal structure. Because of the two-dimensional structure of the heating and its symmetry in x, the model domain is taken to be confined to the positive x direction ($0 < x < 200$ km) and all derivatives in the y direction vanish.

For the benchmark heating, the amplitude is taken to be $\delta Q = 6$ kJ m^{-3} that corresponds to a surface warming of about 6 K. The heating has a horizontal width $a = 10$ km, vertical depth $d = 10$ km, duration $\tau = 300$ s, and is elevated 1 km above the lower boundary $h = 1$ km. Figure 1 shows the temporal and spatial structure of the heating. The total net heating amounts to 150×10^9 J m^{-1}. The heating is turned on slowly, reaching a maximum heating rate at 150 s, where it begins to decrease until it is turned off at 300 s. Because the duration of the heating is comparable to the acoustic cutoff period, no significant vertically propagating acoustic waves are generated. The heating is centered at $x = 0$ km and its magnitude decreases monotonically in the horizontal. The heating is symmetric in the vertical with a maximum at a height of 6 km above the lower boundary. The sensitivity of the model to these choices of heating parameters is examined in section 5d.

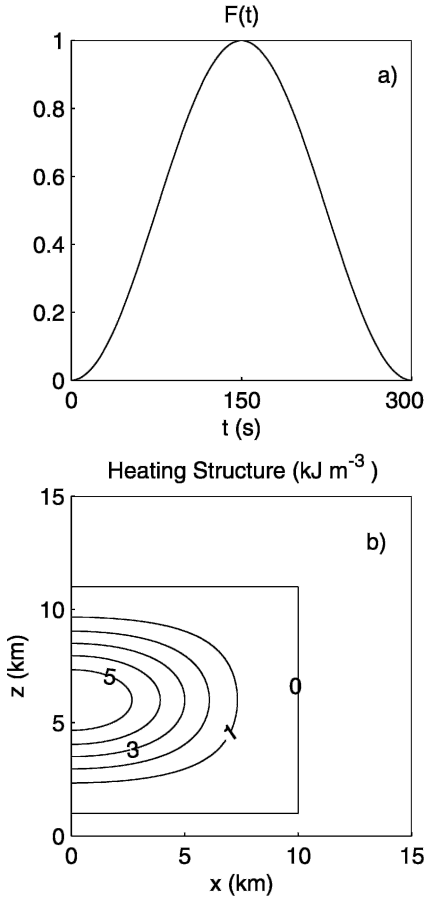

FIG. 1. Heating structure (a) in time and (b) in space. The amplitude is 6 kJ m^{-3}. The heating is confined to a layer 10 km deep and is placed 1 km above the lower boundary. For the benchmark simulation, the width of the heating is $a = 10$ km and its duration is $\tau = 300$ s.

c. Initial conditions

Three different initial conditions are used in this study. For each the atmosphere is at rest in hydrostatic balance. The first is an isothermal hydrostatic atmosphere defined by

$$T_s = T_*, \quad p_s = p_* \exp(-z/H_s),$$

$$\rho_s = \rho_* \exp(-z/H_s),\ \theta_s = \theta_* \exp(\kappa z/H_s), \tag{2.11}$$

where T_*, p_*, $\theta_* = T_*$, and ρ_* are constants satisfying the ideal gas law and Poisson's relation at the surface $z = 0$. Here, $H_s = RT_s/g$ is the density scale height and $\kappa = R/c_p$. The parameter settings are $f = 10^{-4}$ s^{-1}, $g = 9.81$ m s^{-2}, $R = 287$ J kg^{-1} K^{-1}, $c_p = 1004$ J kg^{-1} K^{-1}, $c_v = 717$ J kg^{-1} K^{-1}, $T_* = 255$ K, $p_* = 1000$ hPa, $\rho_* = 1.37$ kg m^{-3}, and $H_s = 7460$ m. The second atmosphere has a surface temperature T_* of 288 K and a constant lapse rate of 6.5°C km^{-1}. The third is similar to the second but has an isothermal stratosphere above 11 km. Figure 2 compares the thermodynamic variables of the three atmospheres used as initial conditions.

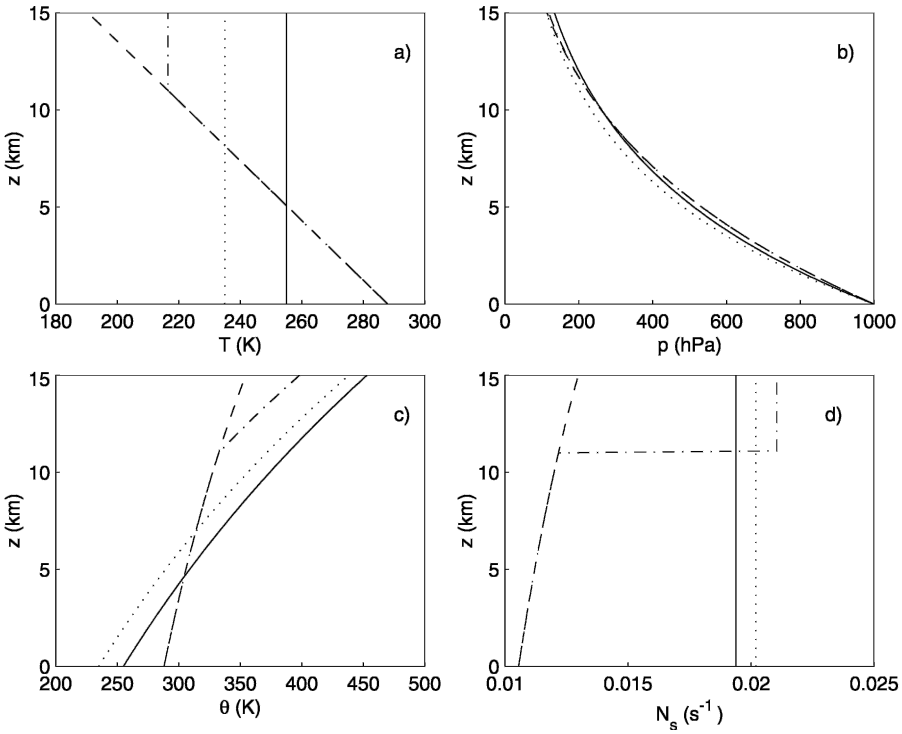

FIG. 2. (a) Temperature, (b) pressure, (c) potential temperature, and (d) buoyancy frequency as a function of height z for the three initial conditions. The solid and dotted curves refer to isothermal atmospheres at temperature 255 and 235 K; the dashed curves refer to the constant lapse rate atmosphere; and the dashed–dotted curves refer to the atmosphere with an isothermal stratosphere.

d. Numerical techniques

Bryan and Fritsch (2002) give a thorough description of the numerical model. The model is integrated with third-order Runge–Kutta time differencing and fifth-order spatial derivatives for the advection terms that are written as the sum of a flux form term and a divergence term. This approach improves the conservation of the variable being advected in the numerical model. The two-dimensional numerical domain is 15 km in height z and 200 km in horizontal distance x. The resolution is 200 m in x and z. The time step is 0.30 s. Although the time splitting feature of the model gives comparable results to those presented here, that feature (along with the associated divergence damping) is not utilized in this study. The boundary conditions are flat rigid horizontal boundaries at $z = 0$ and 15 km where the vertical velocity is set to zero. At the origin $x = 0$, a mirror boundary condition is applied so that the thermodynamic variables and the vertical velocity are symmetric about the origin and the horizontal velocity is asymmetric. At $x = 200$ km, an open boundary condition is employed following Durran and Klemp (1983).

e. Comparison with a linear analytic model

To test the numerical model, the atmospheric adjustment to a 1-K warming applied over five minutes in an initially isothermal atmosphere is solved with both the numerical model and the linear analytic model of Chagnon and Bannon (2005a). In this comparison, variations of the density, temperature, and potential temperature are ignored in the forcing (2.7) to be consistent with the linear model and the net maximum warming is 1 K. In addition, the horizontal structure of the forcing (2.8) is replaced with the horizontal structure

$$H(x) = \frac{1}{1 + x^2/a^2}, \tag{2.12}$$

where $a = 4$ km and, in (2.9), $h = 1$ km and $d = 4$ km in a 10 km by 200 km model domain with grid resolution of 100 and 200 m in x and z, respectively. Visual comparison of the flow fields (not shown) between the two simulations after ten minutes shows no discernible quantitative difference. The root-mean-squared (rms) errors for the horizontal and vertical velocity, pressure, and potential temperature fields are given in Table 1

TABLE 1. Rms error and absolute value of the maximum departure from the base state of horizontal and vertical velocity, pressure, and potential temperature at time $t = 10$ min for the comparison of the numerical nonlinear model with an analytic linear model.

Field	Rms error	Maximum value
u'	2.9×10^{-3} m s^{-1}	4.1×10^{-1} m s^{-1}
w'	5.0×10^{-4} m s^{-1}	1.1×10^{-1} m s^{-1}
p'	9.5×10^{-2} Pa	1.1×10^{1} Pa
θ'	1.5×10^{-3} K	2.4×10^{-1} K

along with the maximum values of the departure from the base-state value of these fields, five minutes after the heating is turned off. These errors are only on the order of 1% of the fields themselves. This result indicates that the numerical model does an excellent job of simulating the linear adjustment process.

3. Energetics

a. Traditional energetics

The equation for traditional energy, te, for a compressible, dry atmosphere is

$$\text{te} = \text{ke} + \text{ie} + \text{pe}, \tag{3.1}$$

where $\text{ke} = \mathbf{u} \cdot \mathbf{u}/2$, $\text{ie} = c_v T$, and $\text{pe} = gz$ are the specific kinetic, internal, and potential energies, respectively. Note that no linear assumptions are made. The inviscid equation for the time rate of change of traditional energy is

$$\frac{\partial \text{te}}{\partial t} = -\mathbf{u} \cdot \nabla \text{te} - \frac{1}{\rho} \nabla \cdot (p\mathbf{u}) + q, \tag{3.2}$$

where q is the heating rate per unit mass that is related to the diabatic warming by

$$\Theta \equiv \frac{\theta}{c_p T} q. \tag{3.3}$$

Similarly, equations for the time rate of change of kinetic, internal, and gravitational potential energy are

$$\frac{\partial \text{ke}}{\partial t} = -\mathbf{u} \cdot \nabla \text{ke} - \frac{1}{\rho} \mathbf{u} \cdot \nabla p + \mathbf{u} \cdot \mathbf{g}, \tag{3.4}$$

$$\frac{\partial \text{ie}}{\partial t} = -\mathbf{u} \cdot \nabla \text{ie} - \frac{1}{\rho} p \nabla \cdot \mathbf{u} + q, \tag{3.5}$$

and

$$\frac{\partial \text{pe}}{\partial t} = -\mathbf{u} \cdot \nabla \text{pe} - \mathbf{u} \cdot \mathbf{g}. \tag{3.6}$$

The heating initially increases the internal energy and, by the ideal gas law, the pressure also increases. As the new pressure gradient forces drive motions, this increase in internal energy is then converted into gravitational potential and kinetic energy.

b. Eulerian available energetics

The Eulerian available energy, ae, (e.g., Bannon 2005) is defined as the difference in the Gibbs function of the atmosphere and a reference state

$$\text{ae} = \Delta h - T_r \Delta s - \alpha \Delta p. \tag{3.7}$$

Here the symbol Δ represents a finite departure from the reference state denoted with the subscript r (e.g., $\Delta p = p - p_r$). The three terms on the right-hand side represent the departure in specific enthalpy $h = c_p T$, the departure in specific entropy $s = c_p \ln\theta$, and the departure in pressure, respectively. Here T_r and p_r are the temperature and pressure of an isothermal reference state and $\alpha = 1/\rho$ is the specific volume. The form of (3.9) allows the partitioning of the available energy into available elastic and available potential contributions, such that

$$\text{ae} = \text{ape} + \text{aee}. \tag{3.8}$$

The Eulerian available potential energy represents the energy associated with the departure of the flow's entropy from the reference entropy and is

$$\text{ape} = h(\theta, \pi_r) - h(\theta_r, \pi_r) - T_r \Delta s, \tag{3.9}$$

where the enthalpy is a function of potential temperature and nondimensional pressure. The Eulerian available elastic energy represents the energy associated with the departure of the flow's pressure from the reference pressure and is

$$\text{aee} = h(\theta, \pi) - h(\theta, \pi_r) - \alpha \Delta p. \tag{3.10}$$

The equation for the time rate of change of Eulerian available energy is

$$\frac{\partial(\text{ke} + \text{ae})}{\partial t} = -\mathbf{u} \cdot \nabla(\text{ke} + \text{ae}) + \left(1 - \frac{T_r}{T}\right) q - \frac{1}{\rho} \nabla \cdot (p'\mathbf{u}). \tag{3.11}$$

Comparison of (3.2) and (3.11) indicates that the traditional total energy changes due to the net rate of working by the total pressure field, $\nabla \cdot (p\mathbf{u})$, and by the heating, but the available total energy changes due to the working by the perturbation pressure $p' = \Delta p$, and by the heating that is modified by the efficiency factor $(1 - T_r/T)$.

Following Bannon (2005), the equations for the time rate of change of Eulerian available potential, available

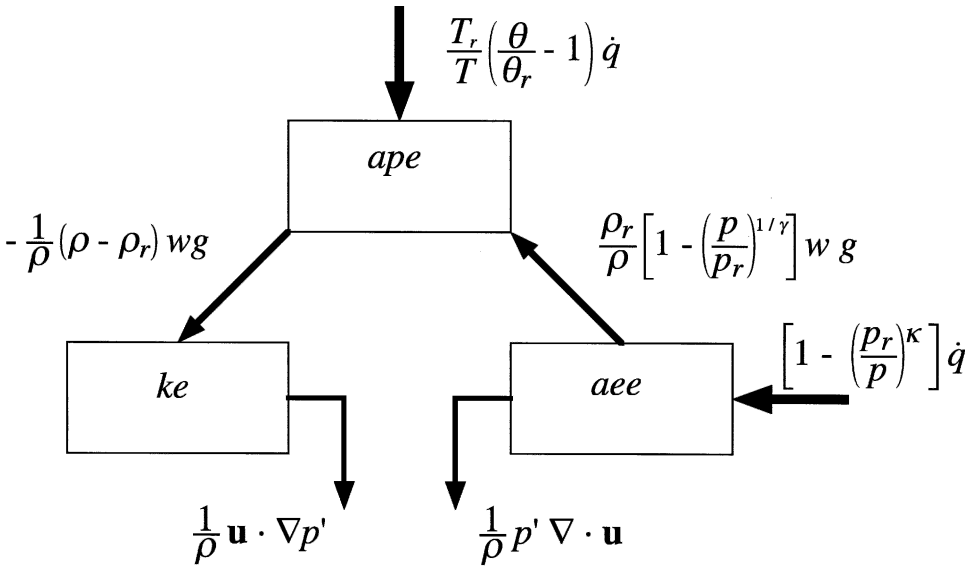

FIG. 3. Schematic box diagram showing the conversion of energy between Eulerian available elastic, available potential, and kinetic energy. The heavy arrows depict generation mechanism; the thin arrows depict conversion mechanisms. The direction of the arrow indicates the direction of positive conversion/generation.

elastic energy, and kinetic energy can be shown to take the form

$$\frac{\partial \text{ape}}{\partial t} = -\mathbf{u}\cdot\nabla\text{ape} + \frac{T_r}{T}\left(\frac{\theta}{\theta_r} - 1\right)q + \frac{\rho_r}{\rho}\left[1 - \left(\frac{p}{p_r}\right)^{1/\gamma}\right]wg + \frac{1}{\rho}(\rho - \rho_r)wg, \tag{3.12}$$

$$\frac{\partial \text{aee}}{\partial t} = -\mathbf{u}\cdot\nabla\text{aee} + \left[1 - \left(\frac{p_r}{p}\right)^{\kappa}\right]q - \frac{\rho_r}{\rho}\left[1 - \left(\frac{p}{p_r}\right)^{1/\gamma}\right]wg - \frac{1}{\rho}p'\nabla\cdot\mathbf{u}, \tag{3.13}$$

and

$$\frac{\partial \text{ke}}{\partial t} = -\mathbf{u}\cdot\nabla\text{ke} - \frac{1}{\rho}\mathbf{u}\cdot\nabla p' - \frac{1}{\rho}(\rho - \rho_r)wg. \tag{3.14}$$

In the above equations, w denotes the velocity component in the z direction and $\gamma = c_p/c_v$. It can be shown that the sum of (3.12), (3.13), and (3.14) yields (3.11) because $T_r\theta/(T\theta_r) = (p_r/p)^{\kappa}$. Figure 3 gives a schematic showing the generation of and conversion between these available energy terms and summarizes the above three equations. The heating generates both available elastic and potential energy. Heating in regions of relatively high pressure (compared to the reference state) will increase the available elastic energy; heating in regions of relatively warm air will increase the available potential energy. Available potential energy is converted into kinetic energy during the descent of relatively dense air. This conversion occurs mainly in the buoyancy waves. Available elastic energy is converted into available potential energy during ascent in regions of relatively low pressure. This conversion occurs mainly in vertically propagating acoustic modes. In the simulations reported here, very little energy is exchanged between these two terms because the heating has a long duration and generates few vertical acoustic waves. Kinetic and available elastic energy each have a sink due to the redistribution of energy within the domain. In a closed system, Eulerian available energy is conserved in the absence of an external forcing.

Bannon (2005) has shown that, in the small amplitude limit, the linear versions of the available potential and elastic energies reduce to

$$\text{ape} \cong \frac{1}{2N_r^2}\left(\frac{g\theta'}{\theta_r}\right)^2, \quad \text{aee} = \frac{p'^2}{2\rho_r^2 c^2}, \tag{3.15}$$

and are thus consistent with linear theory. Here $c = \sqrt{\gamma RT}$ is the speed of sound and $N_r^2 = \text{g d}(\ln\theta_r)/dz$ is the square of the buoyancy frequency.

4. Atmospheric adjustment in an isothermal base state

This section presents an analysis of the numerical model solutions to the benchmark heating of Fig. 1 in an isothermal base-state atmosphere described by

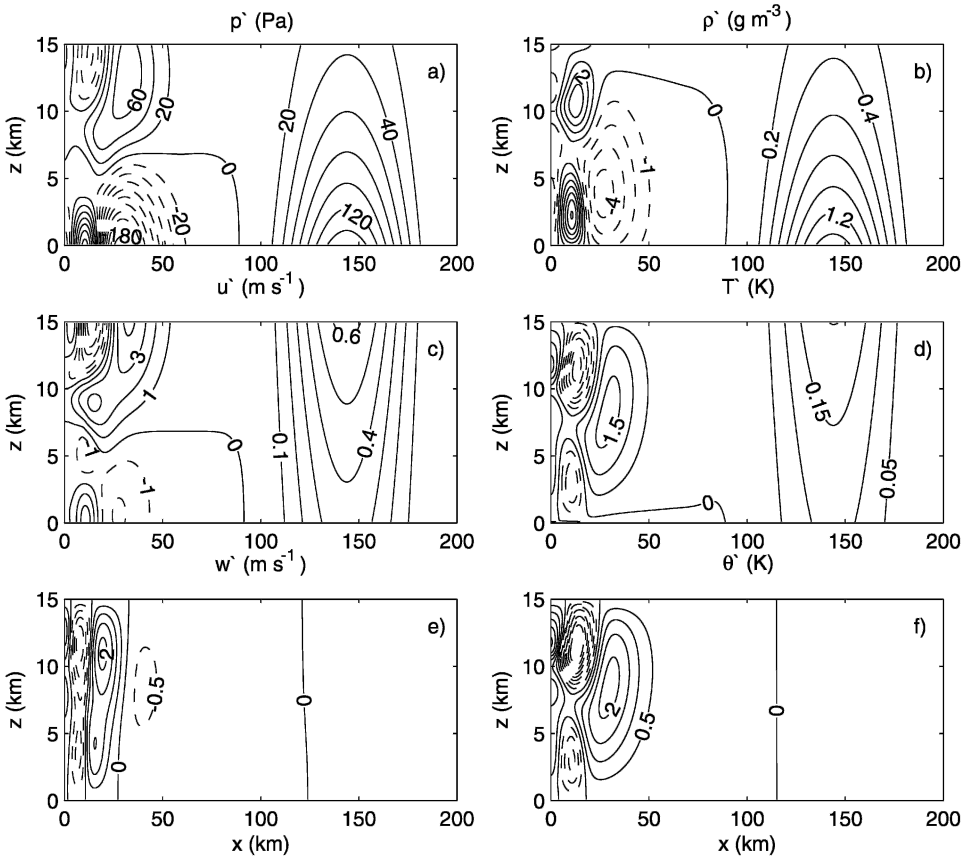

FIG. 4. Perturbation flow fields at time $t = 10$ min of (a) pressure in Pa, (b) density in g m^{-3}, (c) velocity in the x direction in m s^{-1}, (d) temperature in K, (e) vertical velocity in m s^{-1}, and (f) potential temperature in K. Here and elsewhere, dashed contours represent negative values. In this and subsequent contour pots, the contour intervals are not uniform; different contour intervals are used to resolve both the Lamb and buoyancy modes.

(2.11). It represents an extension of the linear analysis of Chagnon and Bannon (2005a,b) to finite amplitude heating.

a. Flow fields

The heating generates both buoyancy waves and Lamb waves that propagate away from the heated region at different speeds. Linear buoyancy waves have a vertical velocity whose vertical structure is given by sin $(n\pi z/D)$ exp $(z/2H_s)$ where $D = 15$ km is the depth of the atmosphere. The group velocity of these waves depends on the vertical wavenumber, n. The $n = 1$ buoyancy mode has the largest maximum horizontal group velocity of 87 m s^{-1}. The $n = 2$ and $n = 3$ modes have maximum horizontal group velocities of 45 and 30 m s^{-1}, respectively. In contrast, the Lamb wave in an isothermal atmosphere has no vertical velocity and travels at approximately (because of the effects of rotation) the speed of sound $c_s = 320$ m s^{-1}.

Figure 4 presents contour plots of several of the perturbation fields at time $t = 10$ min, or 5 min after the heating has ended. Here, perturbation refers to the difference between a field and its initial condition and is denoted by a prime. Because of their differences in group velocity, the various waves have dispersed and are distinguishable at difference distances from the heating. A Lamb wave packet is seen in the plots beyond $x = 100$ km. This packet creates positive anomalies in the pressure, density, temperature, and u fields centered around $x = 140$ km. The maximum pressure perturbation is 154 hPa and lies along the lower boundary. The maximum density perturbation also falls along the lower boundary; however, the maximum value of u is along the upper boundary with a value of 0.63 m s^{-1}. This positive u field implies that the packet leads to a net outward expansion of the environment (see Chagnon and Bannon 2005a, Fig. 9a). Finally the packet has a weak, positive temperature perturbation whose maxi-

mum value lies along the upper boundary and is on the order of 0.20 K. The width of this wave packet is approximately equal to the speed of sound multiplied by the duration of the heating (96 km) and is wider than the 10-km horizontal scale of the heating. This packet also leaves a trailing wake of weak negative winds in the v field (not shown) on the order of a few centimeters per second due to Coriolis deflection of the u velocity. Because Lamb waves are hydrostatic in an isothermal base-state atmosphere, there is no vertical velocity and thus no potential temperature perturbation is associated with them.

Figure 4 also shows the buoyancy modes as anomalies in the vertical velocity (Fig. 4e) and potential temperature (Fig. 4f) fields within 60 km of the heating. Linear theory (e.g., Chagnon and Bannon 2005a) is helpful in interpreting these fields. After the Lamb waves, the lowest vertical wavenumber buoyancy mode is the first to emerge from the heated region. As this $n = 1$ mode passes, the air sinks, resulting in the advection of higher base-state values of potential temperature downward toward the lower boundary. This is the signal of compensating subsidence in the environment outside the region of the heating (Bretherton and Smolarkiewicz 1989) with inflow near the surface and outflow aloft. Trailing this first mode is the $n = 2$ mode that is characterized by sinking air at the surface and rising air aloft. This dipole is also seen in the potential temperature field, as a positive anomaly at low levels and a negative anomaly at upper levels. The structure of the $n = 2$ mode is partially masked in Figs. 4e and 4f by the superposition of slow moving $n = 1$ modes. The $n = 3$ mode has rising air at the surface, sinking air at mid level, and rising air aloft. As higher vertical wavenumber modes pass, we see more complicated patterns of inflow and outflow, both at the surface and aloft (Chagnon and Bannon 2005a). The buoyancy modes also create perturbations in the pressure, density, and horizontal velocity fields, which alternate in sign as the waves pass by.

A plot of the velocity vector field (u, w) around $x = 10$ km at $t = 10$ min (not shown) reveals a cyclonic rotor below 5 km centered at $z = 2$ km that is similar to that depicted in Fig. 7c of Chagnon and Bannon (2005a). This structure can be inferred from the contour plots of u and w in the lower left corner of Figs. 4c and 4e around $x = 10$ km and $z = 5$ km.

b. Potential vorticity and mass conservation

Figure 5 shows the global integral of both density and density-weighted potential vorticity. Here Ertel's potential vorticity q takes the form

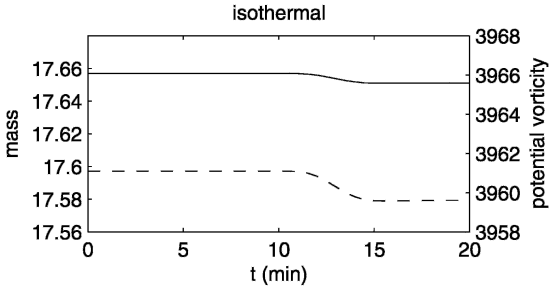

FIG. 5. Global integrals of mass (solid curve) in 10^9 kg and density-weighted potential vorticity (dashed curve) in K m s^{-1} as a function of time t.

$$q = \frac{1}{\rho}\left(f + \frac{\partial v}{\partial x}\right)\frac{\partial \theta}{\partial z} - \frac{1}{\rho}\frac{\partial v}{\partial z}\frac{\partial \theta}{\partial x} \tag{4.1}$$

in the two-dimensional model. Figure 5 indicates that both quantities remain conserved during the model integration for the first ten minutes. In particular, although the heating alters the distribution of the potential vorticity (see below), it does not alter the global potential vorticity. After that time, a small amount of mass exits the domain due to a positive density anomaly within the Lamb packet. Similarly there is also a slight decrease in potential vorticity as the Lamb packet exits the domain around time $t = 12$–14 min. This decrease is due to the weak negative perturbations in the v field contributing to the first term in Eq. (4.1), but is several orders of magnitude smaller than the potential vorticity anomaly within the heated region. In contrast, linear theory predicts no potential vorticity associated with a Lamb wave.

Examining the evolution of the perturbation potential vorticity dipole (Fig. 6) within the heated region also emphasizes the difference between the linear and nonlinear solutions. This dipole is a result of the vertical symmetry of the heating. Below the center of the heated layer the vertical gradient of the heating is positive, which increases the vertical gradient of potential temperature. This results in an increase in potential vorticity. Above the center of heating the vertical gradient of the heating is negative, which decreases the potential temperature gradient. This creates a negative potential vorticity anomaly. The global integral of this dipole is zero because the heating does not extend to the boundaries of the domain.

Figure 6 shows the evolution of the potential vorticity anomaly following the heating. Over time, the dipole becomes distorted due to horizontal and vertical advection. The inflow at the surface compresses the positive perturbation in the horizontal; the outflow aloft stretches the negative perturbation. After 30 min how-

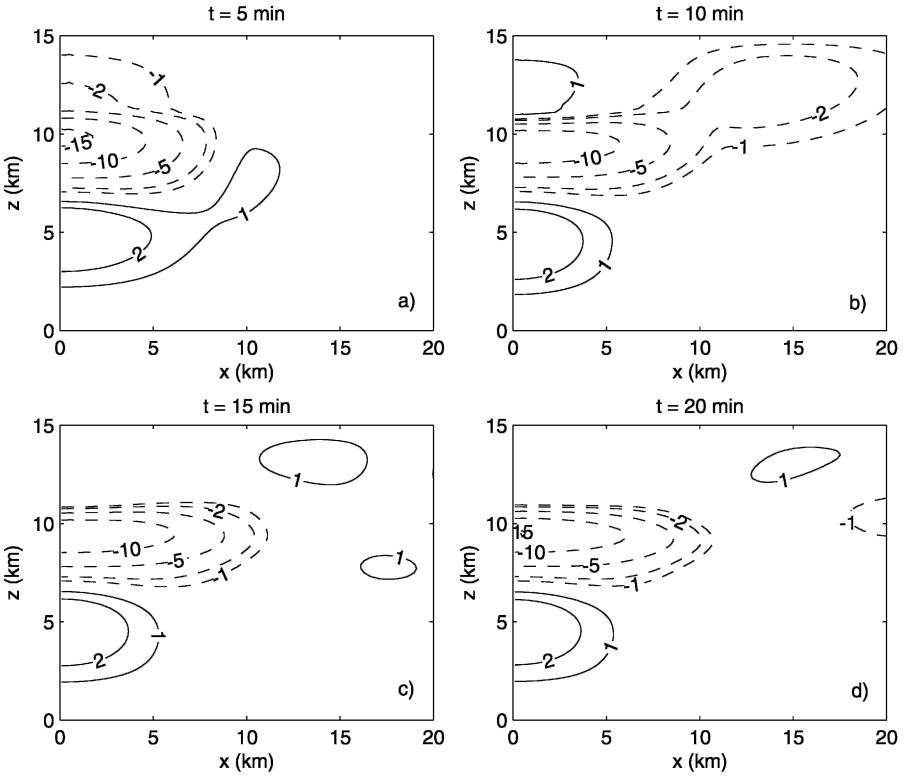

FIG. 6. Potential vorticity perturbation at time (a) $t = 5$ min, (b) $t = 10$ min, (c) $t = 15$ min, and (d) $t = 20$ min. Contour intervals are $\pm(1, 2, 5, 10, 15, \ldots) \times 10^{-7}$ K m^2 s^{-1} kg^{-1} and the zero contour is omitted.

ever, this potential vorticity dipole still remains within the heated layer. While a similar dipole is present in the linear solution, it does not evolve with time. The ultimate steady state will be a hydrostatically and geostrophically balanced flow consistent with the distribution of potential vorticity.

c. Energetics

This section compares and contrasts the traditional and Eulerian available energetics using column integrated values [see Bannon (2005) for a discussion of the vertical variation of the energetics]. Specifically the density weighted vertical integrals of the specific energies are denoted with capitals. For example,

$$\mathrm{KE} = \int_0^D \rho \mathrm{ke}\, dz, \quad \mathrm{PE} = \int_0^D \rho \mathrm{pe}\, dz,$$

$$\mathrm{APE} = \int_0^D \rho \mathrm{ape}\, dz. \tag{4.2}$$

A common term to both formulations is the kinetic energy, which is plotted in Fig. 7 as a function of horizontal distance x and time t. Superimposed on the contours are dashed lines whose slopes are the inverse of the maximum horizontal group velocities based on linear theory for the Lamb and buoyancy modes. The Lamb wave signal has a small positive slope and the buoyancy waves have progressively larger slopes as the wavenumber n increases. One can readily identify the partitioning of the kinetic energy among the waves with the Lamb waves having the least and the buoyancy having the most.

Figure 8 shows column-integrated values of the perturbation (i.e., departure from the initial condition) kinetic energy, internal energy, and potential energies in the traditional energetics. The change in kinetic energy is several orders of magnitude smaller than the change in both the internal and gravitational potential energies. Furthermore, a large amount of energy propagates away from the heated region in the Lamb packet. This finding is in agreement with Nicholls and Pielke (2000) who performed a numerical simulation of moist convection. They found that the net change in internal and gravitational potential energies within the Lamb waves was approximately equal to the amount of energy added to the system. It is shown below that the Lamb wave packet contains more total traditional energy, te,

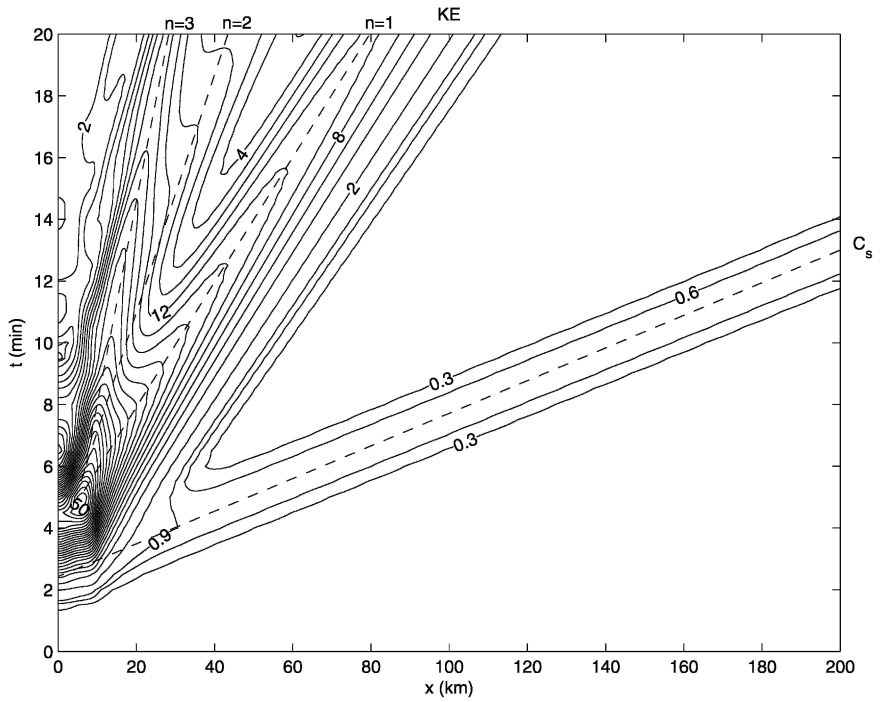

FIG. 7. Column-integrated values of perturbation kinetic energy as a function of distance x and time t. Contours are in kJ m^{-2}. The dashed lines from the ordinate represent the path of a Lamb mode emanating from the time of maximum heating at $t = 150$ s and the paths of the various buoyancy modes emanating from the time $t = 270$ s for $n = 1$ and $t = 240$ s for $n = 2$ and 3.

than that input to the atmosphere by the heating. Despite the fact that Lamb waves contain no vertical motion, there is perturbation potential energy associated with the Lamb packet due to the local compression of the air parcels and an increase in density (Fig. 4b) at fixed heights.

Figure 9 shows column-integrated values of each term comprising the Eulerian available energy (3.7), as well as the total available energy. The reference temperature is that of the initial isothermal atmosphere 255 K. The Lamb packet is characterized by a positive departure in enthalpy (Fig. 9a) because it has a positive temperature perturbation associated with it. Because the pressure perturbation within the packet is also positive, the last term in Eq. (3.7) is a negative contribution (Fig. 9c) to the total Eulerian available energy. There is no contribution from the entropy term (Fig. 9b) because there are no vertical motions, and thus no potential temperature perturbations associated with the Lamb wave in an isothermal atmosphere. Note the large cancellation of the enthalpy and pressure departures in the total available energy (Fig. 9d).

The $n = 1$ buoyancy mode is characterized by a positive temperature and negative pressure perturbation. The air is also sinking, resulting in a positive potential temperature perturbation. Because the temperature anomaly is positive, the change in enthalpy will also be positive. The positive potential temperature perturbation results in a positive entropy departure (Fig. 9b), thus the second term on the right-hand side of Eq. (3.7) will be negative. Finally the negative pressure anomaly results in a positive contribution from the last term in (3.7) (Fig. 9c). Higher-order buoyancy modes have alternating behavior in their energetics relative to the $n = 1$ mode.

Figure 10 shows column-integrated values of the available elastic and available potential energy terms using (3.9) and (3.10). Most of the available elastic energy (Fig. 10b) resides in the Lamb mode and all of the available potential energy (Fig. 10c) is found in the buoyancy modes. This result is in agreement with the available energy partitioning from the analytic solution of linear theory (Chagnon and Bannon 2005b). Eulerian available energy is a positive definite quantity with the majority existing in the buoyancy modes (Fig. 10c), which is also in agreement with linear available energy. Therefore, Eulerian available energy provides us with a formulation that can be used to diagnose the energetics of atmospheric adjustment to finite-amplitude heatings in a manner similar to linear theory.

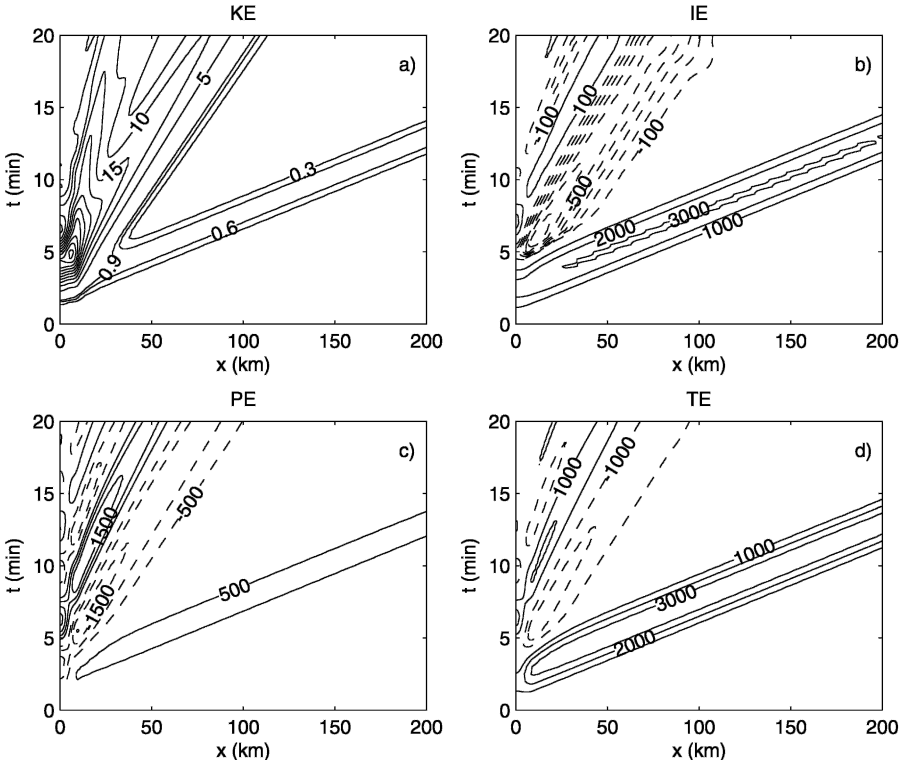

FIG. 8. Column-integrated values of perturbation (a) kinetic (KE), (b) internal (IE), (c) potential (PE), and (d) total traditional energy (TE) plotted as a function of distance x and time t. Contours are in kJ m^{-2}.

Figure 11 presents a comparison of the domain-integrated traditional and available energetics as a function of time. Figure 11a shows the domain integral of each term of traditional energetics. The effect of the heating is primarily to increase the internal energy of the model atmosphere and secondarily to increase the potential energy. In comparison to the total energy, the kinetic energy is relatively insignificant. The majority of the total energy propagates away from the heated region with the Lamb packet and the total perturbation energy becomes negative as the packet exits the domain around time $t = 12$–14 min. The decrease in potential and internal energy is due to the net lateral expansion and, hence, cooling of the atmosphere produced by the Lamb packet in its wake. This result implies that the Lamb wave packet contains more total traditional perturbation energy (186×10^9 J m^{-1}) than that input to the atmosphere by the heating (150×10^9 J m^{-1}).

Figure 11b gives the domain-integrated values of Eulerian available energy. The effect of the heating is primarily to increase both the kinetic and available potential energies equally with only a minor increase in the available elastic energy. Thus the majority of the available energy added to the system during the heating is projected onto the buoyancy waves and the steady state associated with the potential vorticity dipole (Fig. 6).

d. Results for a negative heating

Results for a cooling (not shown) with $\delta Q = -6$ kJ m^{-3} produce flow fields similar to those for a warming but of opposite sign. The Lamb wave packet is one of contraction that leaves behind a warmer atmosphere of greater mass, greater total traditional energy, and greater potential vorticity. The potential vorticity dipole has a reversed sign with the upper region deeper and narrower than that for a warming. Similarly the lower region is shallower and broader than that for a warming. These structural changes reflect the reversal of the transverse circulation and the associated horizontal and vertical advections. The energetics for the cooling case is similar to that displayed in Fig. 11 for a warming but the sign of the internal, potential, and total energies are reversed in Fig. 11a. The sign of the available energy terms remain positive.

5. Atmospheric adjustment in nonisothermal base states

This section presents an analysis of the numerical model solutions to the heating of Fig. 1 in the constant

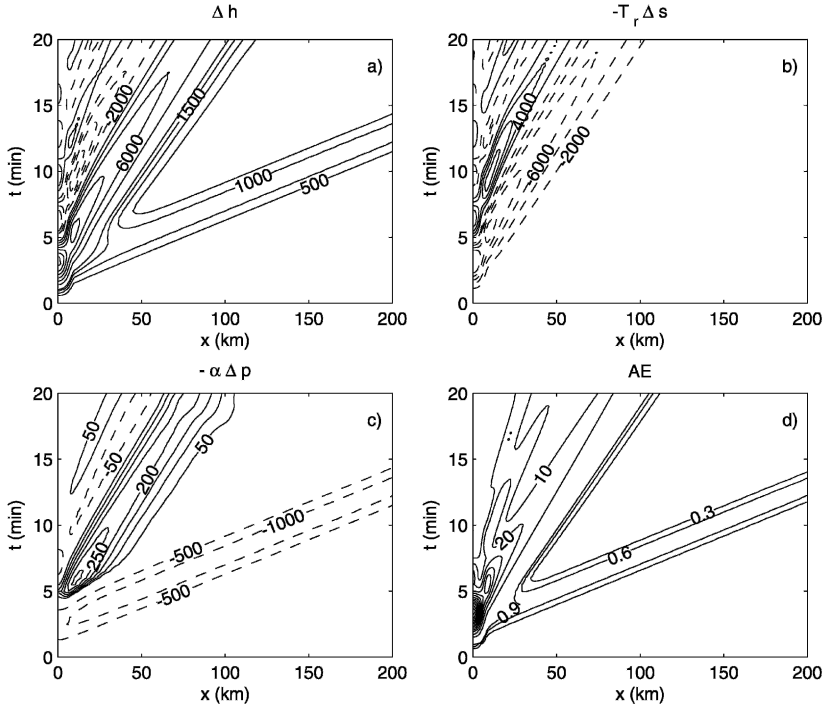

FIG. 9. Column-integrated values of (a) departure in enthalpy, Δh, (b) departure in entropy multiplied by the reference temperature, $-T_r\ \Delta s$, (c) departure in pressure multiplied by specific volume, $-\alpha\ \Delta p$, and (d) total Eulerian available energy (AE): (a)–(c) represent each of the three terms in the equation for Eulerian available energy (2.7). Contours are in kJ m^{-2}.

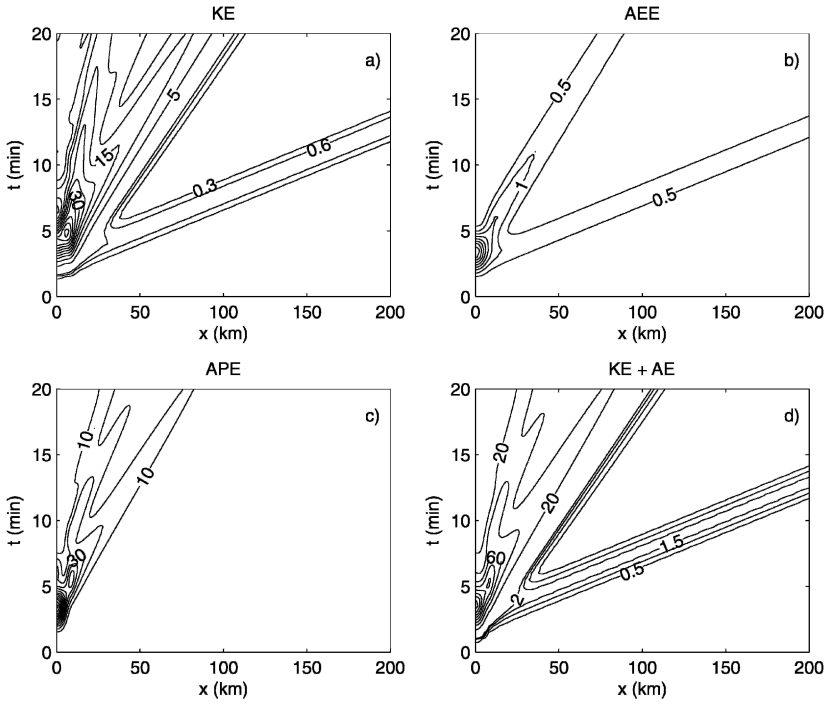

FIG. 10. Column-integrated values of perturbation (a) kinetic, (b) Eulerian available elastic (AEE), (c) Eulerian available potential (APE), and (d) total kinetic and Eulerian available energy (KE + AE). Contours are in kJ m^{-2}.

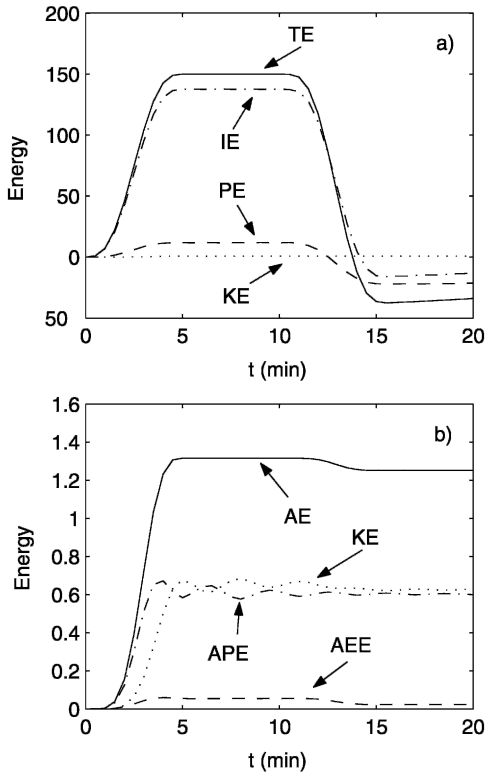

FIG. 11. Domain integrals of perturbation (a) traditional energetics in 10^9 J m^{-1} and (b) Eulerian available energetics in 10^5 kJ m^{-1} as a function of time.

lapse rate and tropopause atmospheres described in Fig. 2.

a. Flow fields

Figure 12 exhibits various flow fields for the atmosphere with a constant lapse rate troposphere and an isothermal stratosphere, henceforth referred to as the tropopause case. Comparison of Fig. 12 with Fig. 4 reveals several qualitative differences in the atmosphere's response to the heating. The Lamb packet in the tropopause case contains vertical motion (Fig. 12e) and, as a result of vertical advection, a potential temperature perturbation (Fig. 12f). This vertical motion is consistent with the analysis of Lamb (1932, sections 311 and 312). Despite these qualitative differences, the other flow fields (Fig. 12a–d) have similar structures and amplitudes. The square of the tropospheric buoyancy frequency in the tropopause case is half of the isothermal case. This reduction in static stability is reflected in the stronger buoyancy mode response in Fig. 12 relative to those of the isothermal case of Fig. 4. The flow fields in the case constant lapse rate case (not shown) are similar to the tropopause case but without the distortion above 11 km.

b. Potential vorticity and mass conservation

The evolution of the domain-integrated mass and potential vorticity (not shown) for the nonisothermal atmospheres are similar to Fig. 5. Both the mass and the potential vorticity drop as the Lamb packet leaves the domain.

Figure 13 depicts the evolution of the potential vorticity for the tropopause case. In the troposphere, the evolution is similar to that of the isothermal case of Fig. 6. Because the inflow and outflow (Fig. 12c) is larger in the tropopause case, the asymmetry in the lateral extent of the upper and lower portions of the dipole is increased. In addition, the larger vertical motions produce a vertical distortion of the dipole. The lower cyclonic portion is stretched vertically while the upper anticyclonic portion is squashed. Lastly, the potential vorticity in Fig. 13 shows large anomalies in the stratosphere associated with large vertical advections of potential temperature (Fig. 12f) as the buoyancy modes propagate from the heated region. The potential vorticity in the constant lapse rate case (not shown) is similar to that of Fig. 13 but with much weaker anomalies above 11 km. Inspection of Table 2 indicates that the potential vorticity dipole is slightly weaker for the nonisothermal atmospheres.

c. Energetics

The evolution of the column-integrated traditional energetics is displayed in Fig. 14 for the tropopause case. The energetics of the Lamb wave packet has a similar amplitude and structure as that of the isothermal case and propagates at a slightly slower speed. The buoyancy modes are larger in amplitude in the tropopause case and, because of the reduced static stability, their horizontal group velocity is significantly reduced. The evolution of the traditional energetics in the constant lapse rate case (not shown) is similar to that of Fig. 14.

The time evolutions of the domain-integrated energies for the nonisothermal atmospheres are similar to that displayed in Fig. 11a and are not shown. In all three cases, the total perturbation energy becomes negative once the Lamb packet exits the domain. Table 3 summarizes the domain-integrated energetics at $t = 10$ min, before the Lamb packet leaves the domain. The reduced static stability in the troposphere of the nonisothermal atmospheres allows for a greater generation of kinetic and potential energies and a reduction in the internal energy. It is noted that the conservation of the total energy is better than that implied by the table because of round-off errors.

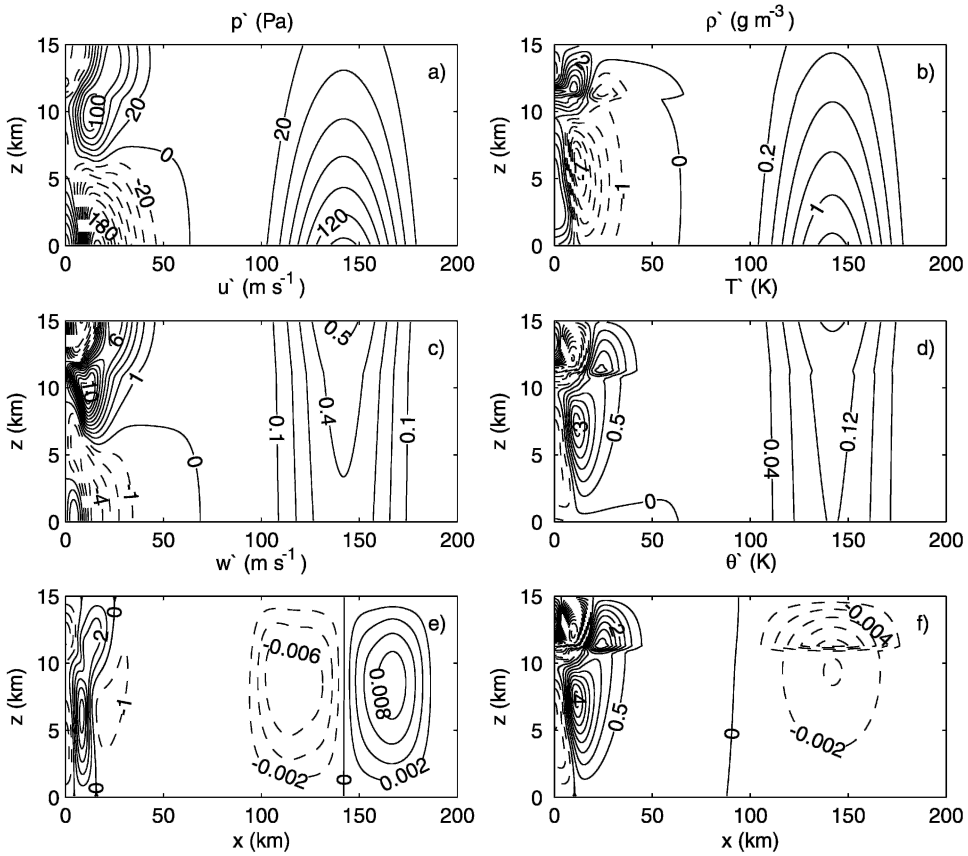

FIG. 12. As in Fig. 4 but for the tropopause case.

Available energetics in the nonisothermal case is hampered by the ambiguity in the choice of the reference temperature T_r. (In the isothermal case, it is natural, though not necessary, to choose the base-state temperature 255 K. That choice, however, ensures that the available potential and elastic energies are initially zero.) In the nonisothermal case, three choices present themselves. One choice is the minimum temperature in the initial sounding. This choice would ensure that the total efficiency factor $(1 - T_r/T)$ of the heating in (3.11) would be nonnegative. A second choice, that of the mean temperature in the initial sounding, would produce negative efficiencies above and positive efficiencies below the level of the mean temperature. A third choice, based on the theory of Livezey and Dutton (1976), is an isothermal temperature of 235 K that has the same mass and total static energy as the initial sounding. This temperature corresponds approximately to a semi-infinite isothermal atmosphere with the same surface pressure and with the same sum of internal and potential energies as the tropopause atmosphere of 15-km depth. Figure 15 shows the evolution of the domain integrated perturbation available energetics for these different choices of the reference temperature. As the reference temperature is increased from the minimum of the initial sounding 216 K (Fig. 15a) to the energy equivalent atmospheric temperature of 235 K (Fig. 15b), there is a monotonic reduction in the total available energy. This reduction continues for a reference atmosphere with the mean temperature of 252 K (Fig. 15c) but the perturbation (i.e., the difference from the initial conditions) is now negative. It is noted that, although the available energy (3.8) is the sum of two positive definite quantities, the perturbation available energy can be negative. Negative values of perturbation available energy are a result of larger initial values when subtracting off the initial state from the available energy at a given time.

The large negative values of perturbation available potential energy in Fig. 15c can be explained with the aid of Fig. 2b. The qualitative relation (3.15) shows that the available potential energy is proportional to the square of the difference of the potential temperature from its reference value at a given height. The initial impact of the heating is to displace the potential temperature fields to the right to higher values. For the

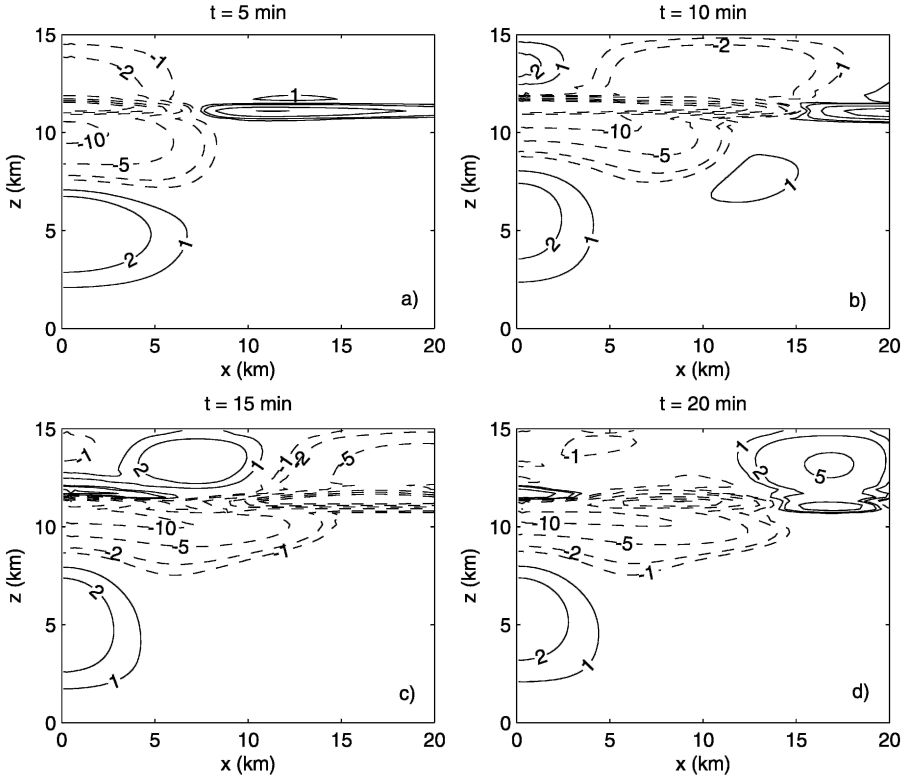

FIG. 13. As in Fig. 6 but for the tropopause case. Contour intervals are $\pm(1, 2, 5, 10, 15, \ldots) \times 10^{-7}$ K m^2 s^{-1} kg^{-1} and the zero contour is omitted.

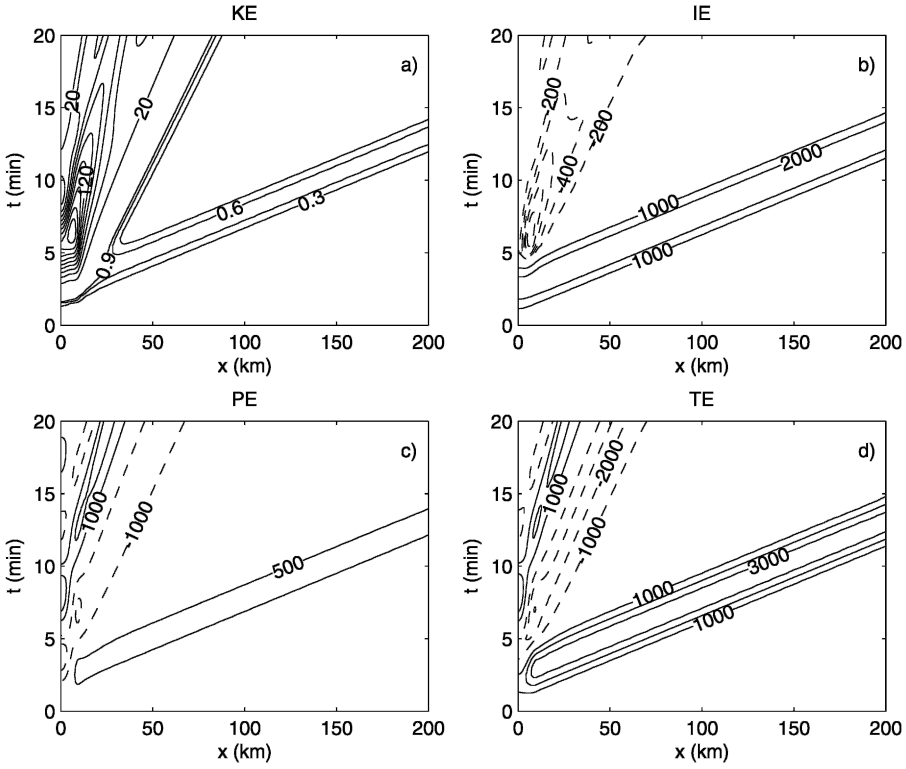

FIG. 14. As in Fig. 8 but for the tropopause case.

TABLE 2. Perturbation potential vorticity extrema associated with the dipole below 11 km for the three atmospheres at time t = 10 min for the benchmark heating. Values are 10^{-7} K m^2 s^{-1} kg^{-1}.

	Isothermal	Constant lapse rate	Tropopause
PV max	3.64	2.83	2.85
PV min	−14.8	−13.6	−13.2

tropopause case (indicated by the dashed–dotted line in Fig. 2b), this displacement will move the potential temperature field toward the reference potential temperature for an isothermal atmosphere of 252 K (indicated approximately by the solid curve in Fig. 2b) above 4.5 km but away from the reference below 4.5 km. Thus, negative perturbation available potential energy is generated above and positive below the intersection height of the two curves. For the 252-K reference atmosphere, the negative dominates the positive generation. For the 235-K reference atmosphere (indicated by the dotted line in Fig. 2b), the intersection height is higher (6.9 km) and the positive generation dominates. The generation will be positive at all heights provided the reference atmosphere's potential temperature is everywhere lower than that of the initial atmosphere. This result is consistent with the efficiency factor (T_r/T) $(\theta/\theta_r - 1)$ for the diabatic generation of available potential energy [see (3.12) and Fig. 3].

It is noted that an arbitrarily cool isothermal reference atmosphere is not permitted. For an isothermal atmosphere of temperature T and depth D, the largest value of the potential temperature is at the top of the domain with the value $\theta_D = T \exp(\Gamma D/T)$ where $\Gamma = g/c_p$ is the adiabatic lapse rate. This maximum takes its smallest value for the temperature $T_f = \Gamma D$ and equals 147 K for the parameter settings of this study. The generation of available elastic energy by the heating is positive in all cases of Fig. 15 because the efficiency factor $[1 - (p_r/p)^\kappa]$ is positive (e.g., compare the solid and dashed–dotted curves of the pressure in Fig. 2c).

Figure 16 depicts the evolution of the column integrated perturbation available energy for the tropopause case for a reference temperature of 235 K. It is emphasized that perturbation here means that the initial vertically integrated values of the available potential (14.2 MJ m^{-2}), available elastic (1.5 MJ m^{-2}), and total available energy (15.7 MJ m^{-2}) have been subtracted from the fields. While the perturbation available energy is positive during the heating, it alternates in sign as various buoyancy modes pass. For example, the negative region of perturbation available potential energy located at x = 50 km at time t = 15 min is due to the subsidence of the n = 1 buoyancy mode. Subsidence produces adiabatic warming and, with reference to Fig. 2b, negative available potential energy is generated above and positive below the intersection height of the potential temperature field with that of the reference. The Lamb wave packet exhibits available potential energy in Fig. 16c because there is vertical motion (Fig. 12e) and potential temperature perturbations (Fig. 12f) for Lamb waves in a nonisothermal atmosphere.

TABLE 3. Domain-integrated perturbation traditional energetics for the three atmospheres at time t = 10 min for the benchmark heating. Units are 10^9 J m^{-1}.

	Isothermal	Constant lapse rate	Tropopause
KE	0.7	2.1	2.1
PE	11.7	12.8	12.5
IE	137.7	135.1	135.3
TE	150.1	150.0	149.9

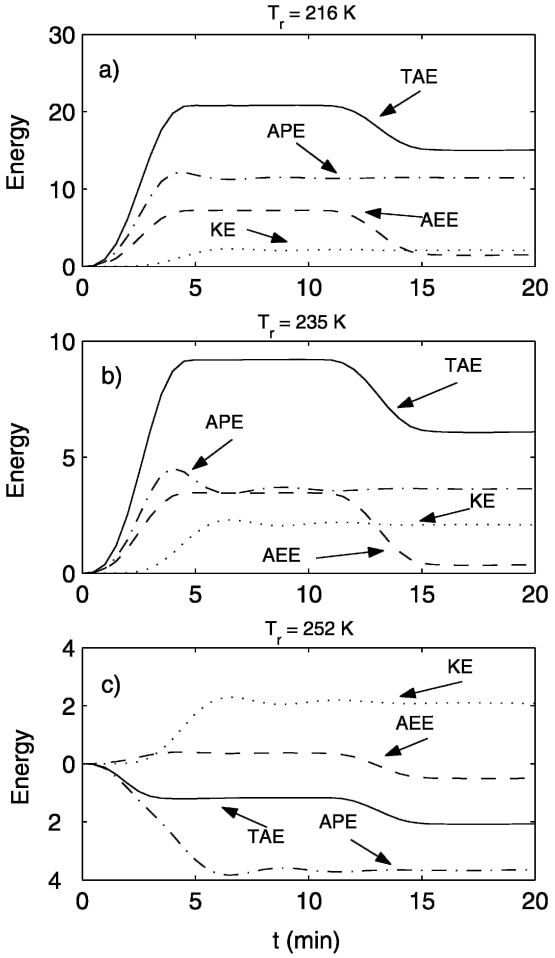

FIG. 15. Domain integrals of perturbation Eulerian available energy in 10^5 kJ m^{-1} as a function of time for the tropopause case for reference temperatures (a) 216, (b) 235, and (c) 252 K.

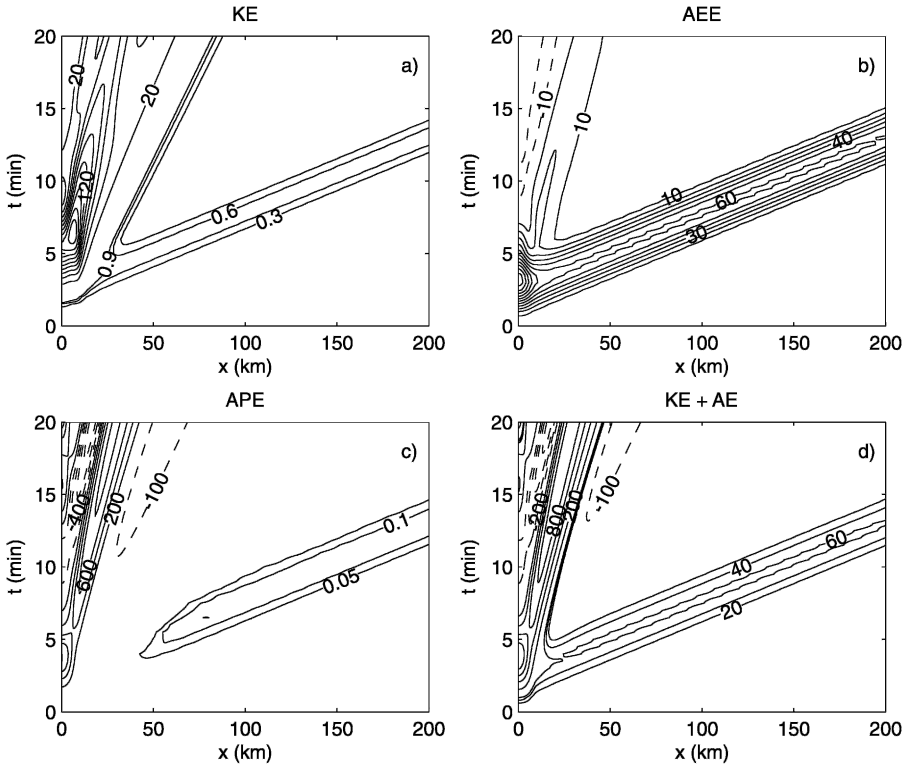

FIG. 16. As in Fig. 10 but for the tropopause case with a reference temperature of 235 K.

d. Sensitivity studies

Tables 4 and 5 summarize the effect of changing the heating amplitude, duration, width, and depth. Each case is for the tropopause atmosphere and the reference atmosphere is isothermal at a temperature of 235 K. In the tables, heating (b) is the benchmark case that has been examined in the experiments discussed to this point. The four other heatings are compared to this benchmark in the discussion below.

Heating (a) is identical to the benchmark but with amplitude reduced by a factor 10. The potential vorticity dipole (Table 4) and all the energies (Table 5) are reduced from the benchmark by roughly a factor of 10 except for the kinetic energy that is reduced by a factor of 100. This reduction in kinetic energy is consistent with it being a quadratic quantity. The fact that the perturbation available elastic and potential energies scale by the factor of 10 is attributed to the fact that they are differences in quadratic quantities.

Comparison of the results for the heatings (a) and (b) allow one to assess the effects of nonlinearity. Contour plots of the fields at 10 min for heating (a) (not shown) are very similar to those of heating (b) (Fig. 12) but reduced by a factor of 10. Figure 17 displays the difference between the fields of heating (b) and those of heating (a) multiplied by a factor of 10. The only significant differences are found in and close to the region

TABLE 4. Perturbation potential vorticity extrema of the dipole for various heatings for the tropopause case at time $t = 10$ min. Values are 10^{-7} K m^2 s^{-1} kg^{-1}.

	Heating				
	(a)	(b)	(c)	(d)	(e)
	$\delta Q = 0.6$ kJ m^{-3} $a = 10$ km $d = 10$ km $\tau = 300$ s	$\delta Q = 6$ kJ m^{-3} $a = 10$ km $d = 10$ km $\tau = 300$ s	$\delta Q = 6$ kJ m^{-3} $a = 10$ km $d = 10$ km $\tau = 150$ s	$\delta Q = 3$ kJ m^{-3} $a = 20$ km $d = 10$ km $\tau = 300$ s	$\delta Q = 12$ kJ m^{-3} $a = 10$ km $d = 5$ km $\tau = 300$ s
PV max	0.285	2.85	2.98	1.60	9.05
PV min	−1.28	−13.2	−12.5	−6.54	−17.7

TABLE 5. Domain-integrated perturbation energetics for various heatings for the tropopause case at time $t = 10$ min. Values are in 10^9 J m^{-1}.

	Heating				
Energy	(a)	(b)	(c)	(d)	(e)
	$\delta Q = 0.6$ kJ m^{-3} $a = 10$ km $d = 10$ km $\tau = 300$ s	$\delta Q = 6$ kJ m^{-3} $a = 10$ km $d = 10$ km $\tau = 300$ s	$\delta Q = 6$ kJ m^{-3} $a = 10$ km $d = 10$ km $\tau = 150$ s	$\delta Q = 3$ kJ m^{-3} $a = 20$ km $d = 10$ km $\tau = 300$ s	$\delta Q = 12$ kJ m^{-3} $a = 10$ km $d = 5$ km $\tau = 300$ s
KE	0.02	2.12	2.38	1.09	2.96
AEE	0.35	3.46	3.49	3.48	3.26
APE	0.43	3.62	3.50	3.98	12.74
KE + AE	0.80	9.20	9.37	8.55	18.96
PE	1.38	12.54	13.92	13.21	21.13
IE	13.60	135.33	133.67	135.68	125.94
TE	15.00	149.99	149.97	150.01	150.03

of the heating. These differences reflect differences in the $n = 3$ and $n = 4$ buoyancy modes. These slowly propagating waves are affected and distorted by zonal winds O (10 m s^{-1}; Fig. 12c). In contrast, the faster moving Lamb and $n = 1$ and $n = 2$ buoyancy modes are unaffected. Two other effects of nonlinearity are (i) the distortion of the steady-state component of the potential vorticity field (Fig. 13) and (ii) a stronger, broader, deeper rotor (not shown, but see Figs. 17c and 17e near $x = 10$ km and $z = 5$ km).

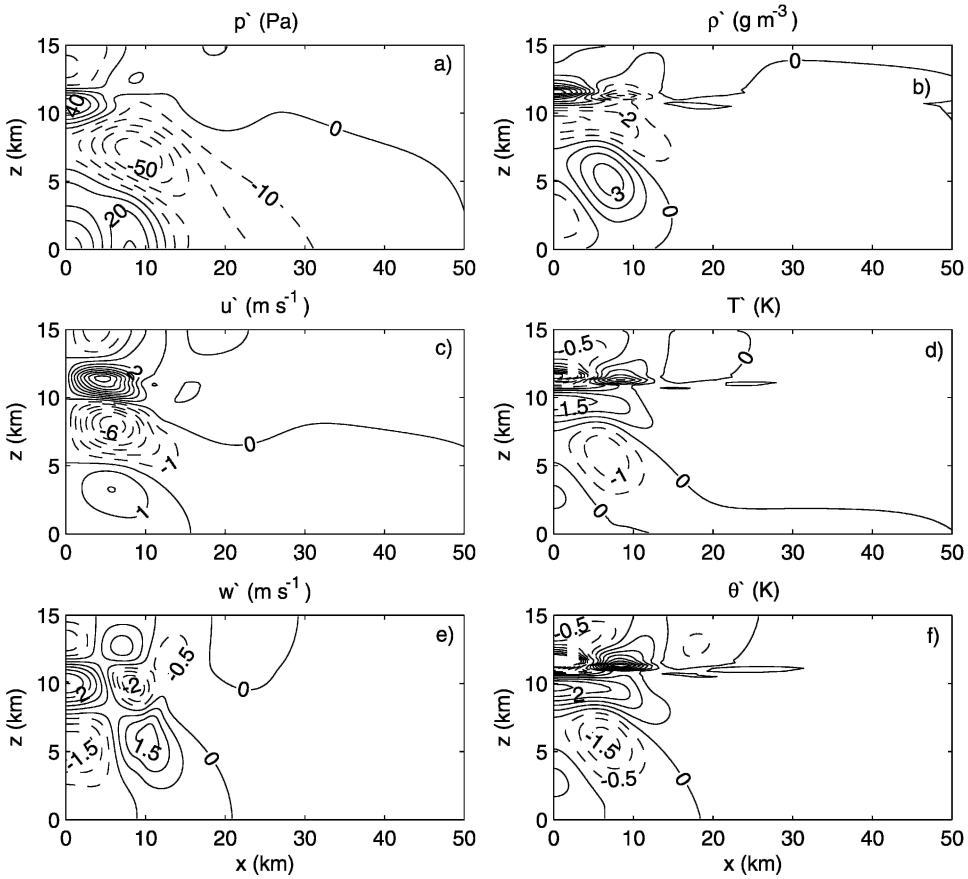

FIG. 17. As in Fig. 4 but for the difference between the fields of the benchmark heating (b) with amplitude $\delta Q = 6000$ J m^{-3} and those of heating (a) multiplied by a factor of 10 with $\delta Q = 600$ J m^{-3}.

For the heating (c) of reduced duration, the kinetic energy is increased slightly with a slight increase in potential energy with a reduction in the internal energy and, hence, in the energy of the Lamb waves. The minimum perturbation potential vorticity is reduced by 10%. For the heating (d) of broader horizontal scale, the kinetic energy is reduced because the pressure anomalies have greater breadth. Similarly, the amplitude of the dipole is reduced. In contrast, a shallower heating (e) has greater vertical gradients and produces stronger vertical motions with increased kinetic and potential energies and a stronger dipole. The shallower heating projects less onto the deep vertical structure of the Lamb waves and the internal energy is reduced.

6. Conclusions

A fully compressible, nonhydrostatic, nonlinear, numerical model has been used to examine the atmospheric adjustment to an external heating. The heating generates a horizontally traveling Lamb wave packet, buoyancy waves, and a steady state rich in potential vorticity. The analysis of the adjustment focused on the flow fields, the potential vorticity distribution, and the energetics of the adjustment. The Lamb and lower-order buoyancy waves generated by the heating are quite similar to those of the linear adjustment. The higher-order buoyancy modes are affected by vertical advections. In addition, the potential vorticity evolves during the nonlinear adjustment due to horizontal and vertical advections. In contrast, the potential vorticity in the linear adjustment is static after the heating has stopped.

Two nonlinear formulations of the energetics provide distinctly different views of the adjustment process. Traditional energy consists of kinetic, internal, and gravitational potential energy. In this formulation, more energy than that added to the atmosphere by the heating propagates away from the heated region at approximately the speed of sound with the Lamb wave packet. As the Lamb packet exits the domain of the model atmosphere, the amount of traditional energy of the system decreases. This decrease is mostly in the internal and gravitational potential energies, indicating that the atmosphere has been cooled and reduced in density by the outward expansion generated by the Lamb packet.

Eulerian available energy consists of kinetic, available potential, and available elastic energy. In contrast to the traditional energetics, the majority of the available energy added to the system during the heating is projected onto the buoyancy waves and the steady state in the form of available potential energy. Most of the available elastic energy propagates away with the Lamb mode. These results are in agreement with linear available energetics.

Examining shorter and longer duration heatings show that the amount of energy projected onto the waves is inversely proportional to the duration of the heating. These findings are in full agreement with Sotack and Bannon (1999) and Chagnon and Bannon (2005b). A larger spatial heating generates a greater amount of both available potential and available elastic energy.

For nonisothermal atmospheres, the available energy is measured as a perturbation from its initial value. This perturbation available energy depends on the choice of the reference temperature and is not necessarily positive definite. It can be negative for sufficiently large values of the reference temperature. The choice of the minimum temperature in the sounding is advocated because it assures that the efficiency factor of the heating in (3.11) is everywhere nonnegative. This choice is consistent with the thermodynamic principle (e.g., Zemansky and Dittman 1981) that the maximum amount of energy available for work is that relative to the coldest reservoir. The results using the perturbation available energy have the same general structure with the majority of the available energy residing in the buoyancy modes. This result demonstrates that this perturbation available energy has utility and enables a direct transition between linear and nonlinear available energetics.

The model used in this study is two-dimensional. This assumption does not severely limit the general relevance of the conclusions presented in this section, but a few caveats should nonetheless be noted. The assumption of horizontal homogeneity in one dimension restricts all divergent motions and the propagation of wave energy to a two-dimensional plane. As a consequence, the wave energy density along a traveling disturbance decays more slowly than in the general three-dimensional case where the energy density decays as the inverse of the square distance from a spherical source. In addition, the structure of the Lamb wave packet in the three-dimensional case is altered to include a trailing region of weak negative perturbation pressure behind the leading edge of strong positive pressure perturbation (Lighthill 1978; Nicholls and Pielke 2000). The energy density of this packet decays as the inverse of the distance from a spherical source.

Acknowledgments. We thank Jeffrey M. Chagnon for helpful discussions and comments on a draft of the manuscript and for providing analytic results, and Richard P. James and George H. Bryan for their help with the numerical model. Adam R. Edson provided assistance with the computations and graphics. The Na-

tional Science Foundation (NSF) under NSF Grant ATM-0215358 provided partial financial support.

REFERENCES

Bannon, P. R., 2005: Eulerian available energetics in moist atmospheres. *J. Atmos. Sci.,* **62,** 4238–4252.

Bretherton, C., and P. K. Smolarkiewicz, 1989: Gravity waves, compensating subsidence, and detrainment around cumulus clouds. *J. Atmos. Sci.,* **46,** 740–759.

Bryan, G. H., and J. M. Fritsch, 2002: A benchmark simulation for moist nonhydrostatic numerical models. *Mon. Wea. Rev.,* **130,** 2917–2928.

Chagnon, J. M., and P. R. Bannon, 2001: Hydrostatic and geostrophic adjustment in a compressible atmosphere: Initial response and final equilibrium to an instantaneous localized heating. *J. Atmos. Sci.,* **58,** 3776–3779.

——, and ——, 2005a: Wave response during hydrostatic and geostrophic adjustment. Part I: Transient dynamics. *J. Atmos. Sci.,* **62,** 1311–1329.

——, and ——, 2005b: Wave response during hydrostatic and geostrophic adjustment. Part II: Potential vorticity and total energy partitioning. *J. Atmos. Sci.,* **62,** 1330–1345.

Durran, D. R., and J. B. Klemp, 1983: A compressible model for the simulation of moist mountain waves. *Mon. Wea. Rev.,* **111,** 2341–2361.

Dutton, J. A., 1973: The global thermodynamics of atmospheric motion. *Tellus,* **25,** 89–110.

Kucharski, F., 1997: On the concept of exergy and available potential energy. *Quart. J. Roy. Meteor. Soc.,* **123,** 2141–2156.

Lamb, H., 1932: *Hydrodynamics*. Dover, 738 pp.

Lighthill, M. J., 1978: *Waves in Fluids*. Cambridge University Press, 504 pp.

Livezey, R. E., and J. A. Dutton, 1976: The entropic energy of geophysical fluid systems. *Tellus,* **28,** 138–157.

Nicholls, M. E., and R. A. Pielke, 2000: Thermally induced compression waves and gravity waves generated by convective storms. *J. Atmos. Sci.,* **57,** 3251–3271.

Sotack, T., and P. R. Bannon, 1999: Lamb's hydrostatic adjustment for heating of finite duration. *J. Atmos. Sci.,* **56,** 71–81.

Zemansky, M. W., and R. H. Dittman, 1981: *Heat and Thermodynamics: An Intermediate Textbook*. 6th ed. McGraw-Hill, 543 pp.